energies

MDPI

Article

Numerical Simulation of Fracture Propagation of Multi-Cluster Perforation and Fracturing in Horizontal Wells: A Case Study of Mahu Oilfield

Baocheng Wu [1], Xinfang Ma [2,*], Jianmin Li [1], Gang Tian [1], Dong Xiong [2], Yushi Zou [2] and Shicheng Zhang [2]

[1] Engineering Technology Research Institute, PetroChina Xinjiang Oilfield Company, Karamay 834000, China; wubc@petrochina.com.cn (B.W.); zy-ljm@petrochina.com.cn (J.L.); tgll2014@petrochina.com.cn (G.T.)
[2] College of Petroleum Engineering, China University of Petroleum-Beijing, Beijing 102249, China; 2021310145@student.cup.edu.cn (D.X.); zouys1985@cup.edu.cn (Y.Z.); zhangsc@cup.edu.cn (S.Z.)
* Correspondence: maxinfang@cup.edu.cn; Tel.: +86-133-6650-5131

Abstract: Mahu oilfield is a typical tight gravel oil reservoir. At present, long-stage multi-cluster fracturing is widely used for reservoir stimulation, and multiple-clusters treatment is realized through cluster perforation. Field monitoring indicates that not all perforation clusters produce hydraulic fractures in the fracturing process, and each cluster of hydraulic fractures in the section will expand unevenly. The unbalanced expansion of multiple clusters of fractures in the section seriously affects the effect of reservoir reconstruction of horizontal wells. Aiming at the long-stage multi-cluster fracturing of horizontal wells, a multi-fracture propagation calculation model considering wellbore flow, performance friction, different fracture criteria at the tip, and the interaction stress among multiple fractures is established in this paper. In order to improve the calculation efficiency, an explicit Runge Kutta Legendre algorithm is proposed to solve the structural mesh, and the solution program is compiled, which provides a basis for the theoretical analysis and rapid solution of the mechanism of multiple fracture growth. Finally, taking Mahu oil field as an example, we calculate the multi fracture propagation and flow distribution under different geological conditions, perforation conditions, and construction parameters. The research results will help to improve the fracturing efficiency of long-stage multi-cluster fractures.

Keywords: conglomerate reservoirs; multi-fracture; competitive propagation; flow distribution; numerical simulation

check for updates

Citation: Wu, B.; Ma, X.; Li, J.; Tian, G.; Xiong, D.; Zou, Y.; Zhang, S. Numerical Simulation of Fracture Propagation of Multi-Cluster Perforation and Fracturing in Horizontal Wells: A Case Study of Mahu Oilfield. *Energies* **2022**, *15*, 5579. https://doi.org/10.3390/en15155579

Academic Editors: Riyaz Kharrat and Reza Rezaee

Received: 23 May 2022
Accepted: 20 July 2022
Published: 1 August 2022

1. Introduction

Mahu oilfield is located in the central area of Mahu sag in the Junggar Basin, which is a super-tight conglomerate reservoir [1]. Hydraulic fracturing and water injection can be used to increase oil and gas production. Hydraulic fracturing is to improve the flow state of reservoir oil and gas by forming artificial fractures and forming fracture networks [2,3]. Waterflooding is another method for increasing oil production in reservoirs. However, waterflooding has the problem of salt precipitation and permeability reduction [4–6]. The reserve scale of the Mahu oilfield is up to 10×10^8 t [7,8], and large-scale cluster fracturing of horizontal wells is widely used in the field [9,10]. The effect of reservoir reconstruction is closely related to the expansion of hydraulic fractures in each perforation cluster. The uneven expansion or non-hydraulic fracture formation of each cluster of fractures in the section may lead to ineffective perforation and affect the final oil and gas production [11].

Because of the complexity of multi-fracture propagation in multi-cluster perforation and fracturing of horizontal wells, many scholars mostly use the numerical simulation method for simulation calculation. The solution model of the multi-fracture propagation model includes boundary element, finite element, extended finite element, and discrete element models [12,13]. Cheng used the displacement discontinuity method (DDM) to

solve the fracture width distribution and stress change during the propagation of multiple parallel fractures but did not consider the real-time propagation of cracks [14]. Olson used the two-dimensional displacement discontinuity model with height correction to calculate the propagation patterns of multiple fractures under constant fluid internal pressure [15]. Based on the model proposed by Olson, Wu considered the perforation friction and the flow equation in the fracture and solved the fluid–structure coupling equation through the Picard iteration [16]. Zeng considered the fluid flow in the wellbore and fractures and coupled the rock mass deformation, established the mathematical model of synchronous propagation of multiple fractures, implicitly solved the crack propagation step by using the asymptotic solution at the crack tip, and solved the model by using the extended finite element method [17]. Based on the quasi-three-dimensional fracture model, Zhao introduced the tip analytical solution and used the Newton–Raphson method to solve the multi-fracture propagation model [18].

These existing studies are only aimed at the simple hydraulic fracture propagation. In the long-stage multi-cluster fracturing, the fluid flow friction, and the interaction in the process of multi-cluster fracture propagation are not considered. These factors are important reasons for the uneven initiation of multi-cluster fractures. Secondly, the fluid structure coupling equations of planar three-dimensional models are usually solved by implicit methods. Although the implicit method is unconditionally stable, the calculation cost is still high. For example, the general calculation example of the implicit level set algorithm takes several days [19]. It is necessary to develop an efficient solution method for planar three-dimensional model to facilitate the application of engineering design.

In this paper, a hydraulic fracture propagation model considering wellbore flow, performance friction and different fracturing criteria at the tip is established for long-stage multi-cluster fracturing of horizontal wells. In order to improve the calculation efficiency, the Runge Kutta Legendre method is used to solve the model, and the calculation results of the model are compared with the PKN analytical solution. In view of the large-scale application of long-term multi-cluster fracturing in Mahu oilfield, taking Mahu oilfield as the background, through compiling calculation programs, the multi-cluster fracture propagation laws and flow distribution laws under different geological conditions and construction parameters are obtained.

2. Theoretical Model of Multi-Cluster Fracture Competitive Propagation

2.1. Model Assumptions

The primary physical processes of multi-cluster fracturing in horizontal wells include: fluid flow in the wellbore, flow distribution among clusters of fractures, competition and expansion of multiple clusters of fractures, fluid filtration to the formation, etc. The primary assumptions of the model are as follows:

(1) The fracture propagation process is quasi-static and satisfies the linear fracture criterion.
(2) The fracture propagates along the plane where the horizontal maximum principal stress is located [18], and the fracture deflection is not considered. Distributed optical fiber monitoring confirms that most of the fracturing fractures are plane fractures [20]. The theoretical analysis of Bunger et al. indicates that the deflection of multiple fractures can be ignored under general mine conditions [21]. McClure further analyzed that plane cracks are suitable for engineering scale crack simulation [22].
(3) The fluid loss from the fracture to the formation is a single-phase one-dimensional flow, and the flow direction is perpendicular to the fracture surface, which can be described by Carter model.
(4) The formation rock mechanical parameters are homogeneous; that is, the young's modulus and Poisson's ratio of a specific reservoir do not change much, and the plane and longitudinal heterogeneity of rock mechanical parameters are not considered.

2.2. Model of Fracturing Fluid Flow in Wellbore and Pore Flow Distribution

The fracturing fluid injected into the wellhead reaches the bottom of the well through the casing (or tubing) and flows into the hydraulic fracture through the perforation. The pressure relationship is as follows [23–25]:

$$p_s = p_c + p_w - p_h \tag{1}$$

where p_s is wellhead pressure, MPa; p_h is the liquid column pressure, MPa; p_c is the friction resistance along the shaft, MPa; p_w is the bottom perforation hole pressure, MPa.

The liquid column pressure of the fluid in the wellbore is calculated according to the fluid density and liquid column height, and its calculation formula is as follows:

$$p_h = \rho g h \tag{2}$$

where ρ is the density of liquid or sand carrying liquid, kg/m^3. The density of the sand-carrying liquid is calculated according to the density and volume fraction of the proppant; h is the height of the liquid column, m.

The flow of fracturing fluid in the wellbore is liquid flow in a circular tube, and the calculation formula of flow friction in the wellbore is [26]:

$$p_c = \int_0^{l_w} f_c(Re, \varepsilon) \frac{1}{D_w} \frac{\rho}{2} V_w^2 ds \tag{3}$$

where D_w is the inner diameter of the fracturing string, m; l_w is the length of the fracturing string, m; ε is the roughness of the inner wall of the fracturing string, m; V_w is the liquid linear flow velocity in the wellbore, m/s; Re is the Reynolds number, $Re = (D_w \rho V_w)/\mu$.

It can be observed from Equation (3) that the friction coefficient f_c along the way is the key to calculating p_c. The friction coefficient f_c is affected by the Reynolds number and the roughness of the inner wall of the string. The friction coefficient along the way can be calculated by Churchill's model [27].

$$f_c = 8\left[\left(\frac{8}{\mathrm{Re}}\right)^{12} + \frac{1}{(\theta_1 + \theta_2)^{1.5}}\right]^{\frac{1}{12}} \tag{4}$$

where θ_1 and θ_2 of the calculation formula is:

$$\begin{cases} \theta_1 = \left[-2.457 \ln\left(\left(\frac{7}{\mathrm{Re}}\right)^{0.9} + 0.27\frac{\varepsilon}{D_w}\right)\right] \\ \theta_2 = \left(\frac{37530}{\mathrm{Re}}\right)^{16} \end{cases} \tag{5}$$

After the injected fracturing fluid reaches the bottom of the well, the fracturing fluid in the wellbore flows into the hydraulic fracture through the perforation. For a horizontal well section with N_f fractures open, the flow of fracturing fluid injected from the wellhead is equal to the sum of the flow into the hydraulic fracture through each perforation.

$$Q_t = \sum_{i=1}^{N_f} Q_i \tag{6}$$

Since the size of the perforation hole is smaller than that of the casing, the friction pressure drop will occur when fracturing fluid flows through the perforation hole. At this time, the following relationship is established:

$$p_w = p_{p,k} + p_{in,k} \tag{7}$$

where $p_{p,k}$ is the perforation friction of fracture k, MPa; $p_{in,k}$ is the inlet pressure of k crack, MPa.

In Formula (8), the perforation friction calculation formula is [28]

$$p_{\mathrm{p},k} = \frac{0.807\rho Q_k^2}{n_k^2 d_k^4 K^2} \tag{8}$$

where n_k is the perforation quantity of k perforation cluster; d_k is the perforation diameter of k perforation cluster, mm; K is the perforation discharge coefficient, dimensionless.

2.3. Flow Model of Fracturing Fluid in Fracture

Theoretical research indicates that the flow of slickwater in the fracture is mainly laminar flow, and turbulent flow may occur only within a few meters of the well. Therefore, for construction fluids such as slickwater, the laminar flow model is adopted to meet the engineering needs. The laminar flow equation is described by the Poiseuille flow theorem, and the fluid flow equation [29] in the crack is as follows:

$$\boldsymbol{q} = -\frac{w^3}{\mu'}\nabla \boldsymbol{p} \tag{9}$$

where $\mu' = 12\mu$, the μ is the hydrodynamic viscosity of the liquid, and Pa·s; q is the volume flow in the joint, m^3/s.

For low permeability formation, the flow of high-pressure fluid in the fracture to the formation can be described by the Carter leakoff model. The Carter leakoff model is derived from the analytical derivation of one-dimensional single-phase parallel flow constant pressure boundary, and its formula is [30]:

$$q_{\mathrm{l}} = \frac{2C_{\mathrm{l}}}{\sqrt{t - t_0}} \tag{10}$$

where C_1 is the filtration coefficient, $\mathrm{m{\cdot}s^{-0.5}}$; t is the injection time, s; t_0 is the time when liquid filtration occurs somewhere in the hydraulic fracture (i.e., the time when the liquid reaches somewhere), s.

Considering the incompressibility of the fluid in the fracture, the continuity equation of the fluid in the fracture is as follows:

$$\frac{\partial w}{\partial t} + \nabla \cdot \boldsymbol{q} + q_{\mathrm{l}} = \delta(\boldsymbol{x} - \boldsymbol{x}_{\mathrm{in},k})Q_k \tag{11}$$

where q_1 is filtration velocity, m/s; Q_k is the injection flow of k fracture, m^3/s; $x_{\mathrm{in},k}$, is the coordinate of the k fracture injection point.

Substituting Equations (9) and (10) into Equation (11) to obtain the transmission equation produces the following:

$$\frac{\partial w}{\partial t} - \nabla \cdot \left(\frac{w^3}{\mu'}\nabla \boldsymbol{p}\right) + \frac{2C_{\mathrm{l}}}{\sqrt{t - t_0}} = \delta\left(\boldsymbol{x} - \boldsymbol{x}_{\mathrm{in},k}\right)Q_k \tag{12}$$

The crack width decreases along the crack length, and the relationship between pressure p and width w in the solid equation is non-uniform. Therefore, Equation (12) is a degenerate nonlocal nonlinear parabolic equation.

2.4. Interaction Stress among Multiple Fractures

Induced stress will be produced in the process of hydraulic fracture propagation. For a radial fracture with a constant internal pressure, the interaction stress perpendicular to the hydraulic fracture surface [31] can be expressed as:

$$\sigma_{I\mathrm{i}} = -\frac{2P_{\mathrm{if}}}{\pi}[C_1^0(r_D, Z_D) - S_0^0(r_D, Z_D) + Z_D C_2^0(r_D, Z_D) - Z_D S_1^0(r_D, Z_D)] \tag{13}$$

where $r_D = r/R_i$, $z_D = z/R_i$, and $Cn\ m$ and $Sn\ m$ denote the integrals as follows:

$$C_m^n(r_D, Z_D) = \int_0^\infty \eta^{n-1} e^{-ZD\eta} J_m(r_D\eta)\cos(\eta)d\eta, S_m^n(r_D, Z_D) = \int_0^\infty \eta^{n-1} e^{-ZD\eta} J_m(r_D\eta)\sin(\eta)d\eta \quad (14)$$

where $J_m(x)$ is a Bessel function of the m order.

Based on Equation (13), Chen [32] provides the final expression of the interaction stress exerted on fracture j by fracture i, which is as follows:

$$\sigma_{Ii}^j = \frac{2}{\pi}\left(\frac{1}{\pi}\frac{E\prime q_i t}{R_I^2}\right)\left[\arctan\left(\frac{R_j}{s_{ij}}\right) - \frac{s_{ij}R_j\left(s_{ij}^2 - R_j^2\right)}{\left(R_j^2 + s_{ij}^2\right)^2}\right]. \quad (15)$$

2.5. Fluid Solid Coupling and Hydraulic Fracture Propagation Model

The crack propagation is a quasi-static process and meets the criteria of linear elastic fracture mechanics [26] as follows:

$$\lim_{d\to 0}\frac{w}{d^{1/2}} = \frac{K'}{E'} \quad (16)$$

where d is the distance from the tip, m; $K' = 4(2/\pi)^{0.5}\ K_{Ic}$, MPa·m$^{0.5}$; K_{Ic} is type I fracture toughness, MPa·m$^{0.5}$; K' is the plane strain Young's modulus, $K' = E/(1 - v^2)$, MPa.

Since the crack tip is the fluid edge, the crack boundary meets the zero-flow condition, that is:

$$\lim_{d\to 0} w^3 \nabla p = \mathbf{0} \quad (17)$$

Introducing dimensionless quantity [33]:

$$\widetilde{K} = \frac{K'd^{1/2}}{E'w}, \widetilde{C} = \frac{4C_l s^{1/2}}{v^{1/2}w}, \widetilde{d} = \frac{\mu V d^2}{12Ew^3}, \widetilde{x} = \frac{\mu V d^2}{12Ew^3}, \chi = \frac{4C_l E'}{K'V^{1/2}} \quad (18)$$

where V is the propagation velocity of the crack tip, m/s.

Using the equation approximation method, the tip control equation is simplified into a differential equation with separable variables:

$$\begin{cases} \frac{d\widetilde{w}}{d\widetilde{x}} = \frac{C_1(\delta)}{\widetilde{w}^2} + \chi\frac{C_2(\delta)}{\widetilde{w}^3}, \delta = \frac{\widetilde{w}}{\widetilde{x}}\frac{d\widetilde{w}}{d\widetilde{x}} \\ \widetilde{w}(0) = 1 \end{cases} \quad (19)$$

Coefficient C_1 and C_2 monotonic change, and the range of change is small, such that $C_1(0) = C_2(0) = 4\pi$, $C_1(1/3) = 10.4$, $C_2(1/3) = 10.2$. Because δ has a small variation range, δ can be taken as a constant first so that the tip differential equation can be transformed into a nonlinear equation. Therefore, Equation (19) can be further transformed into the nonlinear equation:

$$\begin{gathered} \widetilde{w}^3 - 1 - \tfrac{3}{2}b\left(\widetilde{w}^2 - 1\right) + 3b^2(\widetilde{w} - 1) - \\ 3b^3\ln\left(\tfrac{b+\widetilde{w}}{b+1}\right) = 3C_1(\delta)\widetilde{x}, b = \tfrac{C_2(\delta)}{C_1(\delta)}\chi \end{gathered} \quad (20)$$

where $\widetilde{b}$, C_1, and C_2 are calculated as follows:

$$\widetilde{b} = \frac{C_1(\delta)}{C_2(\delta)} \quad (21)$$

$$C_1(\delta) = \frac{4(1-2\delta)}{\delta(1-\delta)}\tan(\pi\delta) \quad (22)$$

$$C_2(\delta) = \frac{16(1-3\delta)}{3\delta(2-3\delta)}\tan\left(\frac{3\pi}{2}\delta\right) \quad (23)$$

According to the superposition principle [34], the discrete equation of pressure in the fracture and hydraulic fracture width is:

$$p(x,t) - \sigma_h(x) = \sum_{i=1}^{n} C(x,t)w(x,t) \quad (24)$$

where n is the total number of units; $P(x,t)$ is the fluid pressure in the joint, MPa; $\sigma_h(x)$ is the fluid pressure in the joint, MPa; C is the plane crack kernel function.

The space term of the transmission equation of Equation (12) is discretized by the straight-line method and the finite difference method, and the first-order differential equation of the flow equation is obtained as follows:

$$\frac{dw}{dt} = [\theta A(w)p + (1-\theta)A(w_0)p_0] + S \tag{25}$$

where w_0 and p_0 are the crack width and pressure distribution of the previous step, respectively. The expressions of $A(w)p$ and S are as follows:

$$\begin{aligned}[A(w)p]_{i,j,k} = \frac{1}{\Delta x}\left[\frac{w_{i+0.5,j,k}{}^3}{\mu\prime}\frac{p_{i+1,j,k}-p_{i,j,k}}{\Delta x} - \frac{w_{i-0.5,j,k}{}^3}{\mu\prime}\frac{p_{i,j,k}-p_{i-1,j,k}}{\Delta x}\right] \\ + \frac{1}{\Delta y}\left[\frac{w_{i,j+0.5,k}{}^3}{\mu\prime}\frac{p_{i,j+1,k}-p_{i,j,k}}{\Delta y} - \frac{w_{i,j-0.5,k}{}^3}{\mu\prime}\frac{p_{i,j,k}-p_{i,j-1,k}}{\Delta x}\right]\end{aligned} \tag{26}$$

$$S_{i,j,k} = \frac{4C_1}{\Delta t}\left(\sqrt{t+\Delta t - t_{0i,j,k}} - \sqrt{t - t_{0i,j,k}}\right) + Q_k(t)\frac{\delta_{ii0.jj0,kk0}}{\Delta x \Delta y} \tag{27}$$

We brought Equation (24) into Equation (25) to obtain the differential equation about the width as follows:

$$\frac{dw}{dt} = Mw = [\theta A(w)(\sigma_h + Cw) + (1-\theta)A(w_0)(\sigma_h + Cw_0)] + S \tag{28}$$

Due to the coupling effect of various physical processes, Equation (28) is a strongly rigid equation, which is usually solved by implicit time stepping. However, the implicit algorithm must solve the highly nonlinear equations iteratively in each time step, and the matrix inversion takes a long time to solve the nonlinear equations. To solve these problems, we use explicit algorithm in the model. Let $\theta = 0$ to obtain the explicit equation

$$\frac{dw}{dt} = [A(w_0)(Cw_0 + \sigma_h)] + S = Mw. \tag{29}$$

For an explicit (forward) Euler finite difference scheme, the timestep must satisfy the Courant–Friedrichs–Lewy (CFL) condition [35], written as:

$$\Delta t_E = \frac{\mu}{E\prime}\frac{\Delta x^3}{\overline{w}^3} \tag{30}$$

The CFL time step has great limitations on the explicit Euler scheme, so a more effective method is needed. In order to improve the calculation speed, the explicit method Runge–Kutta–Legendre (RKL) is used in this paper.

3. Model Solving and Validation

3.1. Algorithm Implementation

As shown in Figure 1, the rectangular structured grid is used for numerical calculation. Firstly, a rectangular grid that can completely cover the range of hydraulic fractures is established. The grid labels i, j, and k are the x, y, and z coordinates of the corresponding grid points. The element size is $\Delta x \times \Delta y$. The center point of the element is the width and pressure solution point, and the boundary of the element is the flow solution position. To capture the fracture propagation boundary, the element types are divided into four types: tip element (At), channel element (Ac), element to be inspected (As), and element not calculated (An). The tip element and channel element are active elements, the element to be checked and the element not to be calculated are inactive elements, and the element to be checked is the element to be activated. The unopened cell adjacent to the tip cell is a pending cell. At each time step, it is necessary to judge whether the cells to be checked meet the expansion conditions to update the cell type of the grid. When the width of the element to be inspected reaches the critical width, it is defined as a tip element, the adjacent unopened element becomes a new pending element, and the adjacent tip element is updated as a channel element.

(1) Input basic parameters: stress distribution, rock mechanics parameters, injection procedure, liquid parameters, cluster number, fracture spacing, etc.;
(2) The distribution of pressure and width in a given initial element is solved analytically;
(3) Calculate the number of time steps and RKL integration steps, and the time steps increase;
(4) Substituting the flow distribution obtained from the wellbore model, RKL is used to solve the fluid solid coupling equation to obtain the new pressure and width in the fracture;

(5) Calculate the wellbore flow distribution until it converges with the flow results of the fracture model in step 4;
(6) Calculate wellhead pressure according to the wellbore model;
(7) Calculate the expansion speed and the critical width of the unit to be checked, check whether the pending unit meets the opening conditions, and update the unit type;
(8) Check whether the time reaches the end of injection. If so, it will end and output the result; otherwise range step 3.

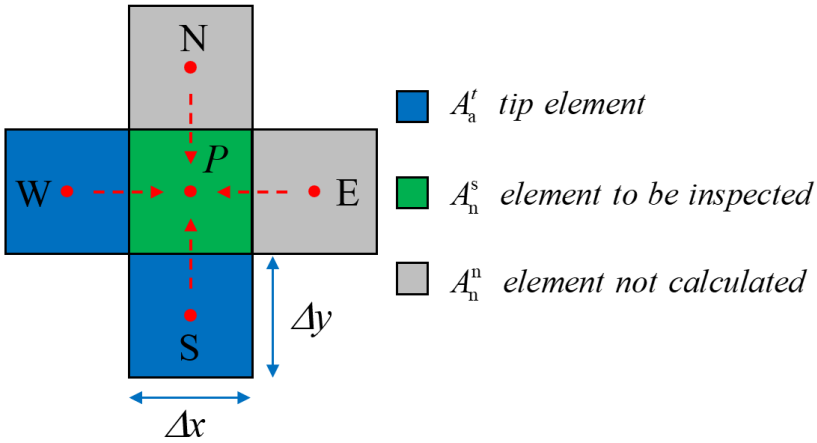

Figure 1. Schematic diagram of element activation and calculation.

3.2. Model Accuracy Verification

The calculation results of the PKN model [36] are verified with the calculation results of the above multi-cluster crack propagation theoretical model. The calculation parameters of the model are as follows, as shown in Table 1:

Table 1. Parameter values.

Input Parameter	Value
Elastic modulus/GPa	30
Poisson's ratio/—	0.25
Fracture toughness/MPa·m$^{0.5}$	0.1
Injection rate/m^3·s^{-1}	0.2
Fluid viscosity/Pa·s	0.01
Time/s	250

Figures 2 and 3 portray the calculation results of the PKN model and multi-cluster crack propagation model in this paper. According to the curve calculation results in the figure, the calculation results of this model are consistent with those of the PKN model, which verifies the correctness of the calculation model and calculation method in this paper.

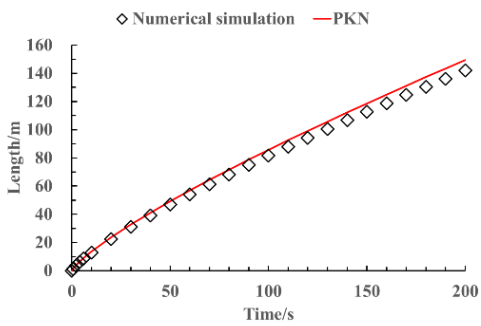

Figure 2. Results of fracture length.

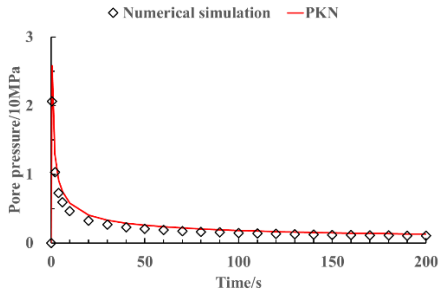

Figure 3. Results of pressure.

4. Numerical Simulation of Multi-Cluster Crack Competitive Propagation

4.1. Model Basic Parameter Setting

Based on the above theoretical model of multi-cluster fracture initiation and propagation of horizontal wells, this section takes the segmented multi-cluster fracturing of horizontal wells in Mahu oilfield in Xinjiang as the background to study the flow distribution of each cluster of perforation holes in the horizontal well section of fracturing fluid and the law of multi-cluster fracture initiation and propagation.

Mahu oilfield is in the central depression of the Junggar Basin, with a depth of 3502 m~3900 m in the middle of the reservoir. Based on the geological and fracturing construction design data of well block Ma 2 and well block Ma 18 in Mahu oilfield, the calculated benchmark parameters are determined as portrayed in Table 2. During the calculation, only one of the parameters is changed, and the other parameters remain unchanged.

Table 2. Basic simulation parameters.

Parameter Name	Value	Parameter Name	Value
Minimum horizontal in-situ stress, MPa	57	Number of perforation holes per cluster	12
Elasticity modulus, GPa	30	Perforation diameter, mm	12
Reservoir thickness, m	12	Fracturing fluid viscosity, mPa·s	8
Horizontal in-situ stress difference, MPa	9	Liquid volume, 10^2 m^3	17
The thickness of the upper compartment, m	6	Number of clusters per stage	6
Stress difference of upper compartment, MPa	8	Pumping rate, m^3/min	12
The thickness of the lower compartment, m	6	Segment length, m	100
Stress difference of lower compartment, MPa	8	Cluster spacing, m	20
Stress difference between clusters, MPa	0	The inner casing diameter, mm	104.8
Fracture toughness, MPa·$m^{0.5}$	1	Wellbore roughness, mm	0.5

To quantitatively evaluate the liquid inflow difference of each cluster of fractures, the liquid inflow difference coefficient based on the standard deviation of liquid inflow distribution of each cluster is defined as follows:

$$S_d = \sqrt{\frac{1}{N_f - 1}\sum_{i=1}^{N_f}\left(\frac{V_i}{V_t} - \frac{1}{N_f}\right)^2} \tag{31}$$

where V_t is the total liquid volume, m^3; S_d is the differential coefficient of liquid inflow of each cluster in the section, dimensionless.

The difference in liquid inlet volume of each cluster in the section indicates the difference in liquid inlet volume of each cluster of fractures and determines the balanced initiation and expansion degree of each cluster of fractures in the section. When the difference of the liquid inflow of each cluster in the section is $S_d < 4\%$, it is considered that the liquid inflow of each cluster is uniform.

4.2. Influence of Geological Conditions on Multi Fracture Propagation

4.2.1. Influence of Interlayer Stress Difference and Reservoir Thickness

Calculate the difference between fracture propagation and liquid inflow under the conditions of reservoir thickness of 6 m, 10 m, 12 m, 14 m, and 18 m and interlayer stress difference of 6 MPa, 7 MPa, 8 MPa, 9 MPa, 10 MPa, 11 MPa, 12 MPa, 13 MPa, and 14 MPa. Figure 4 portrays several groups of typical fracture propagation patterns under the conditions of different reservoir thickness

and interlayer stress differences, and Figure 5 demonstrates the difference in the liquid inflow of each cluster of fractures under different conditions. When the reservoir thickness is more than 12 m, the difference coefficient of fluid inflow of each cluster of fractures is greater than 4%. There is an uneven fluid inflow in each cluster of fractures, and the uneven expansion of multiple fractures is obvious, which indicates that the length of perforation cluster fractures at both ends is longer than that in the middle. When the thickness of the reservoir is 6 m, the difference in the liquid inflow of each cluster of perforation holes is greatly affected by the difference in interlaminar stress. The difference in interlaminar stress ranges from 6 MPa to 14 MPa, and the different coefficient of liquid inflow increases from 3.8% to 4%. In general, the uneven liquid inflow of each perforation cluster is obvious when the reservoir thickness exceeds 12 m. When the reservoir thickness is less than 6 m, the liquid inflow of each cluster is affected by the interlayer stress difference.

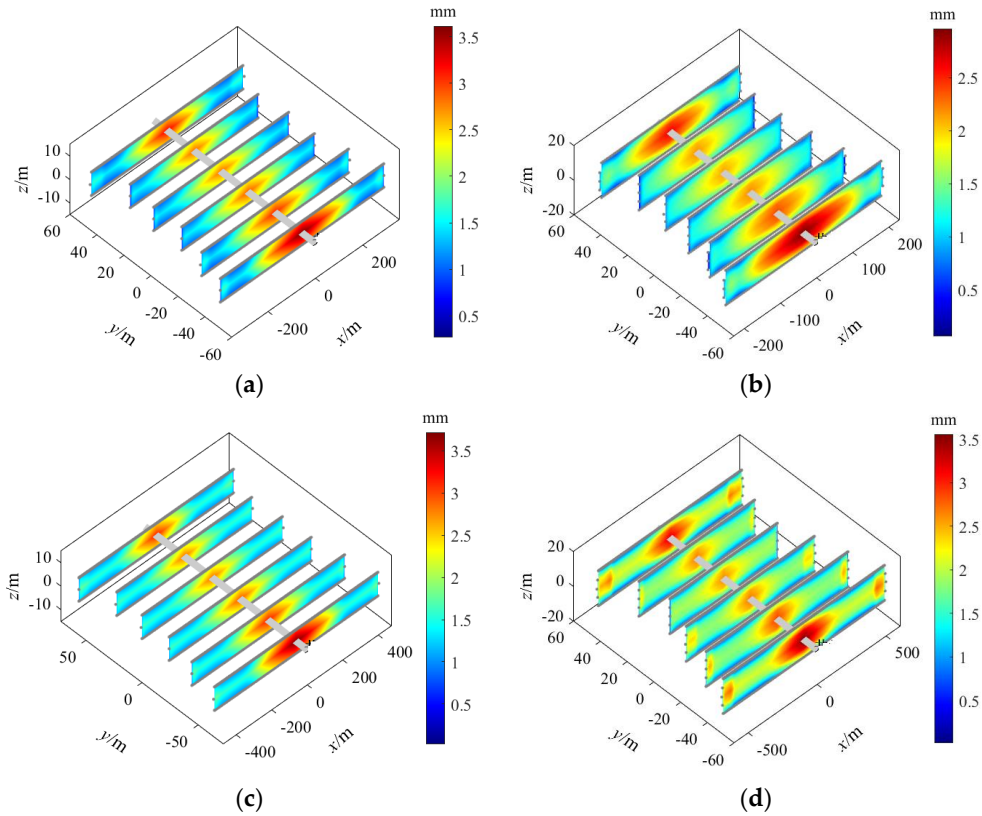

Figure 4. Multi-fracture propagation pattern under different reservoir thickness and interlayer stress difference. (**a**) 6 MPa, 10 m; (**b**) 6 MPa, 12 m; (**c**) 10 MPa, 10 m; (**d**) 10 MPa, 12 m.

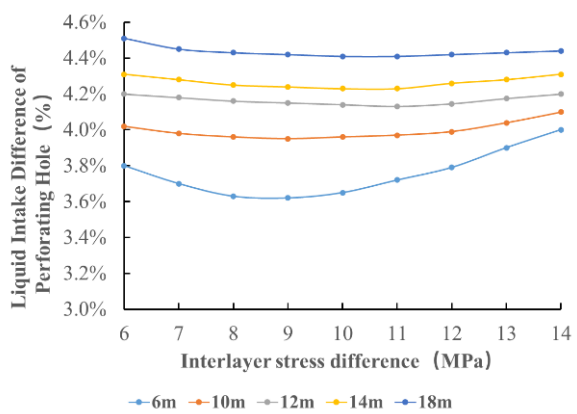

Figure 5. Effect of different reservoir thickness on stress difference between lower layers.

4.2.2. Effect of Stress Difference between Clusters

Stress data from the Mahu field indicate that there is a difference in minimum horizontal stress at different locations between perforating clusters. This difference has an impact on cluster fracture propagation. We calculated the crack propagation when the stress difference between clusters was 0–5 MPa and the liquid inlet difference at the heel end, middle, and toe end in the section. Figure 6 portrays several groups of typical fracture propagation patterns under the conditions of different reservoir thickness and inter-cluster stress differences, and Figure 7 portrays the difference in the fluid inflow of each cluster fracture under the conditions of different inter-cluster stress differences. With the increase of the stress difference between clusters, the multi-cluster cracks gradually form non-uniform crack initiation and expansion, and the non-uniform liquid inflow of each cluster is obvious. When the stress difference between clusters is 1 MPa, all perforated clusters produce hydraulic cracks. With the increase of the stress difference between clusters, when the stress difference between clusters is 2 MPa and 3 MPa, the crack propagation at the toe end is restrained. When the stress difference between clusters reaches 4 MPa, there is no crack at the toe end.

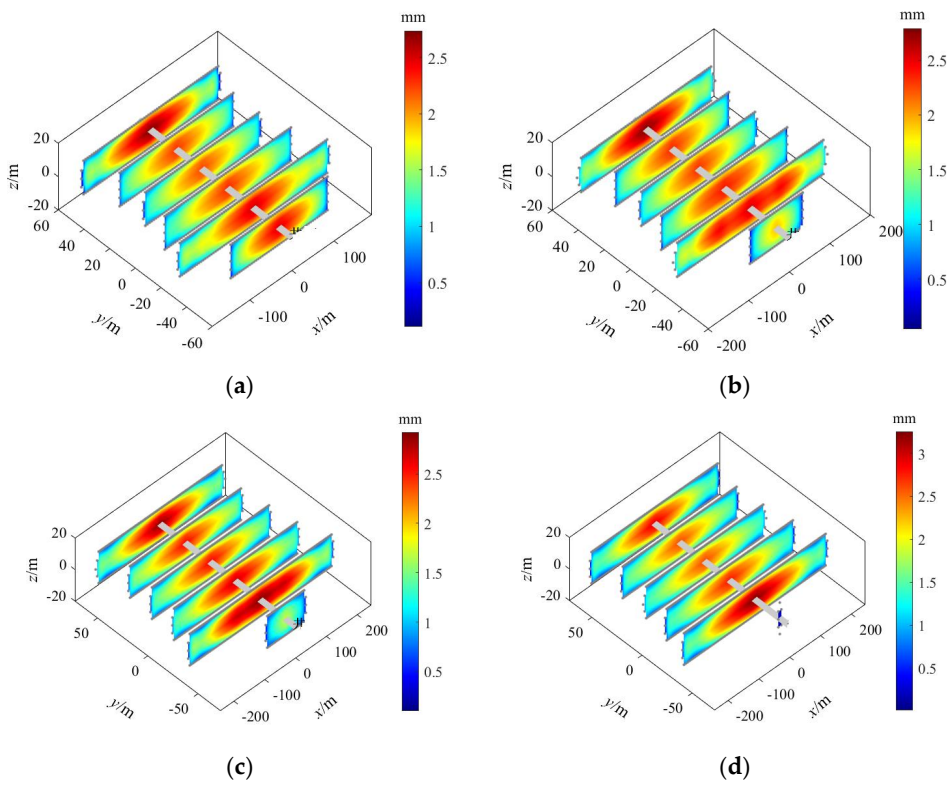

Figure 6. Multi-crack propagation pattern under different stress differences between clusters. (**a**) 1 MPa; (**b**) 2 MPa; (**c**) 3 MPa; (**d**) 4 MPa.

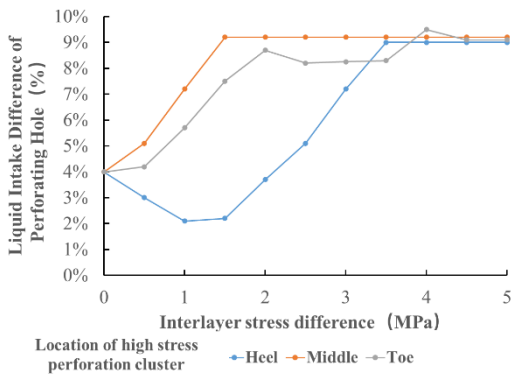

Figure 7. Liquid inflow difference of multiple clusters of cracks under different stress differences between clusters.

From the difference in liquid inflow under different stress differences between clusters, with the increase in a stress difference between clusters, the difference in liquid inflow at the heel of the well, middle part, and toe of the well will increase. When the stress difference between clusters reaches 3.5 MPa, the liquid inflow difference of multi-cluster cracks is more than 8%, which is not conducive to the balanced initiation and expansion of multi-cluster cracks in the section.

4.3. Influence of Construction Parameters on Multi Crack Propagation

4.3.1. Influence of Single-Segment Cluster Number

The fluid inflow of multiple clusters of fractures is greatly affected by the number of clusters in a single section. The fracture propagation and the fluid inflow of each cluster with the number of clusters in a single section from 2 to 12 are calculated, respectively. Figure 8 portrays several groups of typical fracture propagation patterns under the conditions of different reservoir thickness and interlayer stress differences, and Figure 9 portrays the difference in the liquid inflow of each cluster of fractures under the conditions of different interlayer stress differences. When a single segment is less than four clusters, the cracks in each cluster begin and expand evenly, and the stress shadow between clusters is small. When the number of clusters in a single segment is more than five, the cracks in each cluster in the segment expand unevenly, the hydraulic cracks at both ends expand further, and the hydraulic cracks in the middle cluster are affected and expand closer. As the number of clusters in a single section increases from two clusters to twelve clusters, the difference in the liquid inflow of each cluster increases by more than 4%. When the number of perforations in a section exceeds five clusters, the difference in liquid inflow will exceed 4%, and the difference in fracture section length of each cluster increases. Therefore, the number of perforation clusters below five clusters in each section will be more conducive to the balanced initiation and expansion of multiple clusters of fractures.

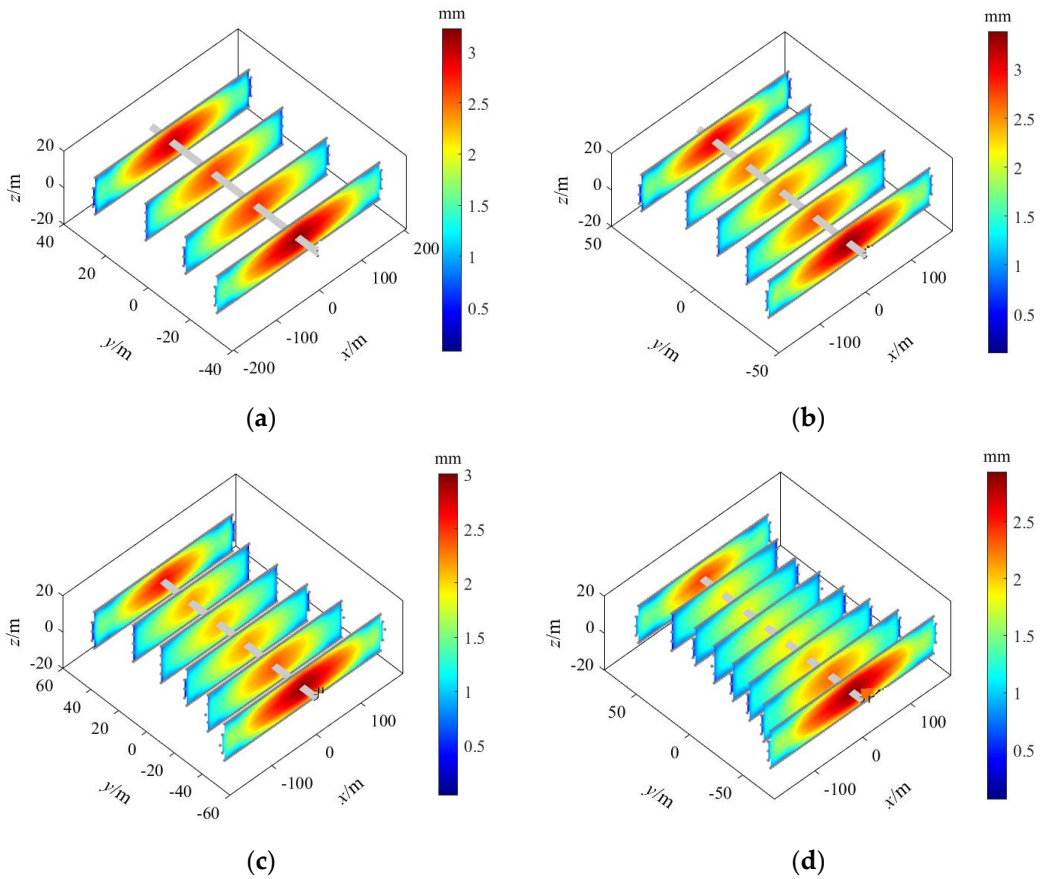

Figure 8. Multi-cluster crack propagation patterns under different cluster numbers. (**a**) 4 clusters, Cluster spacing 20 m; (**b**) 5 clusters, Cluster spacing 25 m; (**c**) 6 clusters, Cluster spacing 20 m; (**d**) 8 clusters, Cluster spacing 15 m.

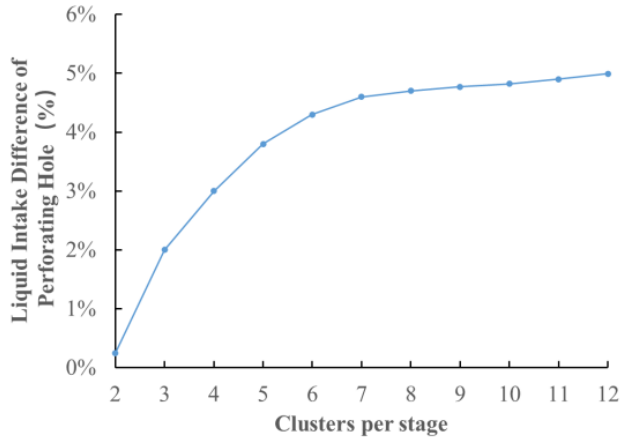

Figure 9. Liquid inflow difference of multiple clusters of fractures under different cluster numbers.

4.3.2. Influence of Perforation Number

We calculated the difference between the fracture propagation and the liquid inflow of each cluster when the number of perforations in a single cluster ranged from two to sixteen. Figure 10 portrays several groups of typical fracture propagation patterns under the conditions of different reservoir thickness and interlayer stress differences, and Figure 11 portrays the difference in the liquid inflow of each cluster of fractures under the conditions of different interlayer stress differences. When the number of perforation holes per shower is three, the crack initiation and expansion of each cluster are uniform. When the number of perforation holes per shower is six, the uneven crack initiation and expansion of each cluster begin to appear. When the number of perforation holes per shower is six, the uneven crack initiation and expansion of each cluster are obvious. Reducing the number of single shower perforation holes can significantly improve the liquid inflow uniformity of each cluster of fractures, from 16 perforation holes/cluster to 6 perforation holes/cluster, and the liquid inflow difference coefficient of each cluster of fractures is reduced by about 6%. The relatively balanced propagation of multiple clusters of fractures can be realized when the number of perforations is less than six. During field construction, it should be considered to reduce the number of perforations per cluster and increase the length of the reconstruction section. For example, in Mahu oilfield, in order to ensure the balanced expansion of multiple clusters of fractures, the average number of perforations per cluster is 3three which is consistent with the simulation results.

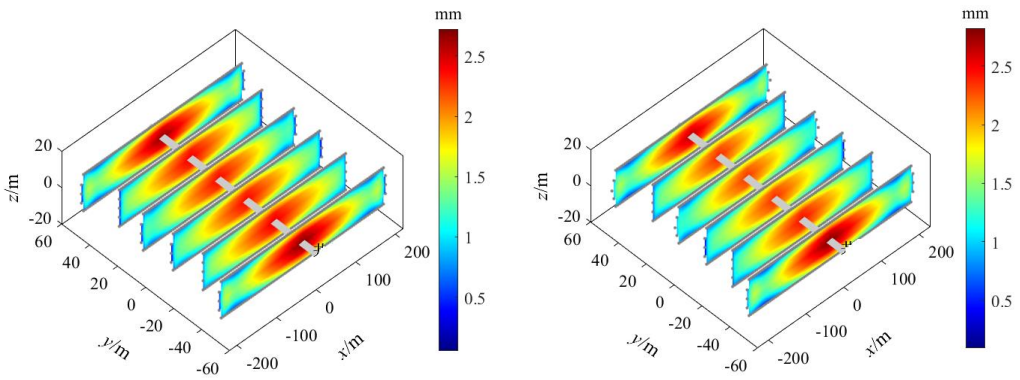

Figure 10. *Cont.*

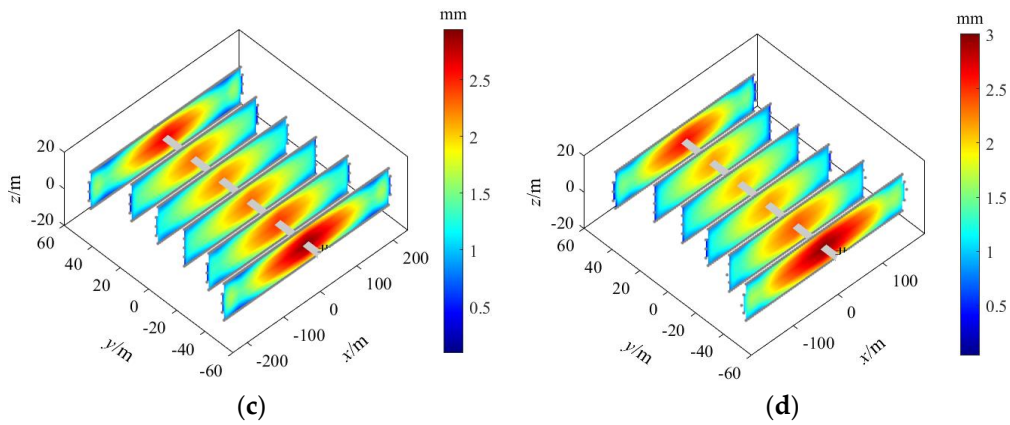

Figure 10. Multiple-fracture propagation patterns under different perforation numbers. (**a**) 3 perforations per cluster; (**b**) 6 perforations per cluster; (**c**) 9 perforations per cluster; (**d**) 12 perforations per cluster.

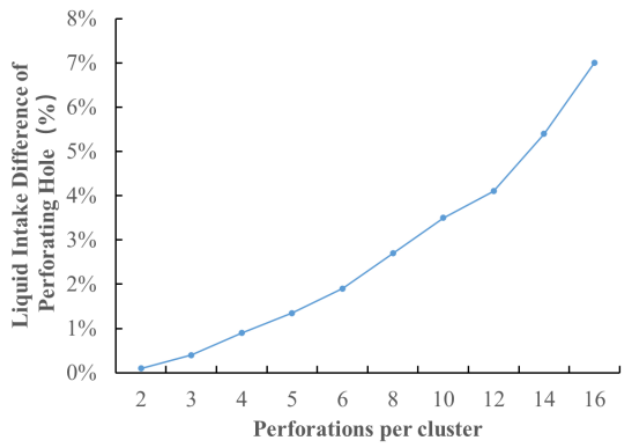

Figure 11. Difference in liquid inflow between clusters under different perforation numbers.

4.3.3. Influence of Perforation Diameter

We calculated the difference between the crack propagation and the liquid inflow of each cluster when the perforation hole was from 6 mm to 22 mm. Figure 12 portrays the fracture propagation patterns of several groups under the conditions of different reservoir thicknesses and interlayer stress differences, and Figure 13 portrays the liquid inflow difference of each cluster of fractures under the conditions of different interlayer stress differences. When the perforation diameter is 10 mm, each cluster of fractures begins to expand unevenly. When the perforation diameter exceeds 10 mm, the degree of uneven expansion intensifies. This is due to the increase in perforation diameter, resulting in the decrease in perforation friction and the significant increase in the different coefficients of fluid inflow of each cluster of fractures. When the pore diameter increases from 6 mm to 12 mm, the differential coefficients of the liquid inlet increase by about 3.4%. When the pore diameter increases from 12 mm to 20 mm, the differential coefficient of the liquid inlet increases to more than 10%.

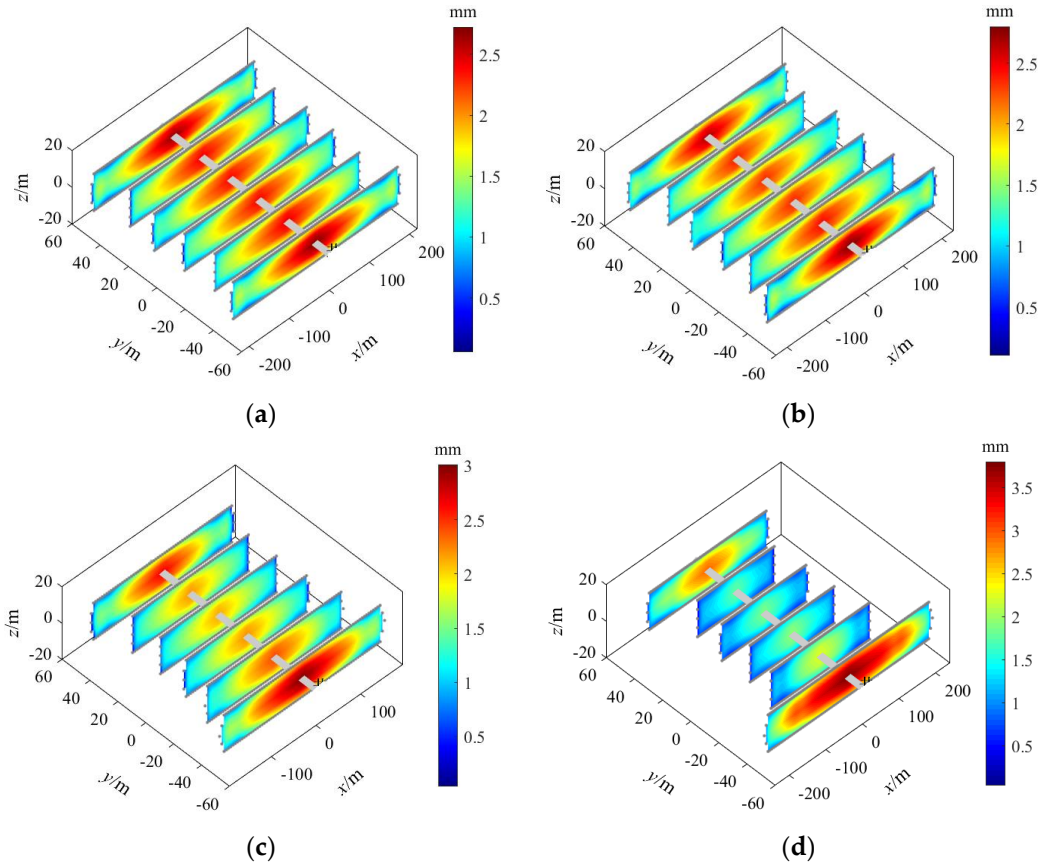

Figure 12. Multi-fracture propagation patterns under different perforation diameters. (**a**) 6 mm; (**b**) 10 mm; (**c**) 14 mm; (**d**) 18 mm.

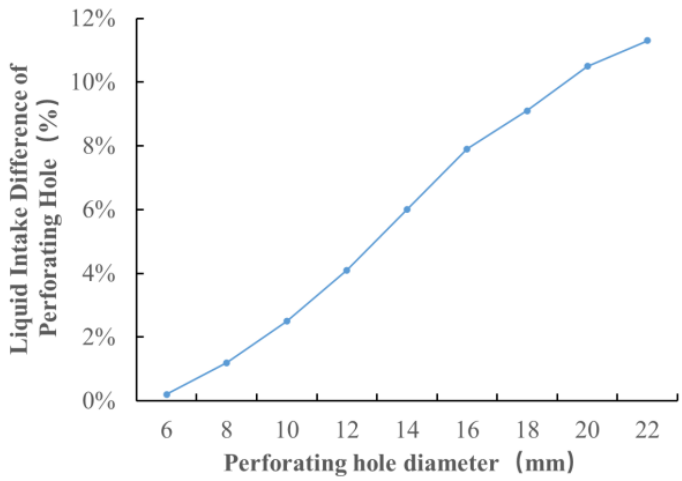

Figure 13. Difference in liquid inflow between clusters under different perforation diameters.

5. Conclusions

In this paper, a multi-fracture propagation model considering wellbore flow, performance friction, different fracture criteria at the tip, and the interaction stress among multiple fractures is established. The explicit Runge–Kutta–Legendre algorithm is used to solve the model to improve the calculation efficiency. Finally, considering Mahu oilfield as an example, the rules of multi-cluster fracture propagation and flow distribution under different geological and construction conditions are simulated. Through the research, the conclusions were as follows:

(1) With the increase of reservoir thickness, the stress shadow effect between multiple clusters of fractures increases, and the difference in the fluid inflow of each cluster of fractures increases.

When the reservoir thickness exceeds 12 m, the difference coefficient of fluid inflow of each cluster of fractures is greater than 4%. There is an uneven fluid inflow in each cluster of fractures, and the uneven expansion of multiple fractures is obvious.

(2) The stress difference between clusters is the key reservoir condition to determine the unbalanced initiation and expansion of multi-cluster fractures. When the stress difference between clusters reaches more than 2 MPa, the unbalanced initiation phenomenon is obvious. When the stress difference between clusters reaches 3.5 MPa, the liquid inlet difference of multi-cluster fractures is more than 8%.

(3) The increase in cluster number, perforation number, and perforation diameter will enhance the uneven degree of fracture propagation in each cluster. The higher the number of clusters in a single section, the more single shower perforation holes, and the larger the perforation diameter, the greater the difference in the liquid inflow of each cluster. The perforation diameters of five clusters/section, six perforation holes/cluster and less than 12 mm are conducive to the relatively balanced expansion of multiple clusters of fractures.

Author Contributions: Conceptualization, B.W.; Data curation, X.M.; Funding acquisition, J.L. and G.T.; Investigation, D.X. and S.Z.; Methodology, X.M.; Project administration, B.W. and X.M.; Software, Y.Z. All authors have read and agreed to the published version of the manuscript.

Funding: This research received no external funding.

Institutional Review Board Statement: The study did not require ethical approval.

Informed Consent Statement: Studies not involving humans.

Data Availability Statement: The study did not report any data.

Conflicts of Interest: The authors declare no conflict of interest.

References

1. Zou, L.Z.; Zou, L.X.; Jiang, X.M.; Liu, Y.B.; Lu, Z.Y.; Li, W.X. The horizontal drilling technology in tight sandy conglomerate reservoirs in Mahu sag. *Xinjiang Oil Gas* **2018**, *14*, 19–24.
2. Zou, C.N.; Pan, S.Q.; Jing, Z.H.; Gao, J.L.; Yang, Z.; Wu, S.T.; Zhao, Q. Shale oil and gas revolution and its impact. *Acta Pet. Sin.* **2020**, *41*, 1–12.
3. Jiang, T.X.; Bian, X.B.; Wang, H.T.; Li, S.; Jia, C.; Liu, H.; Sun, H. Volume fracturing of deep shale gas horizontal wells. *Nat. Gas Ind.* **2017**, *37*, 7. [CrossRef]
4. Khormali, A.; Petrakov, D.G.; Farmanzade, A.R. Prediction and inhibition of inorganic salt formation under static and dynamic conditions effect of pressure, temperature, and Mixing Ratio. *Int. J. Technol.* **2016**, *7*, 943. [CrossRef]
5. Sassan, H.; Wu, X.R.; Catherine, A. Scale formation in porous media and its impact on reservoir performance during waterflooding. *J. Nat. Gas Sci. Eng.* **2017**, *1*, 188–202.
6. Shabani, A.; Kalantariasl, A.; Parvazdavani, M.; Abbasi, S. Geochemical and hydrodynamic modelling of permeability impairment due to composite scale formation in porous media. *J. Pet. Sci. Eng.* **2019**, *176*, 1071–1081. [CrossRef]
7. Hou, Q.J.; He, H.Q.; Li, J.Z.; Yang, T. Recent progress and prospect of oil and gas exploration by Petro China Company Limited. *China Pet. Explor.* **2018**, *23*, 1–13.
8. Jia, C.Z.; Zou, C.N.; Yang, Z.; Zhu, R.; Chen, Z.; Zhang, B.; Jiang, L. Significant progress of continental petroleum geology theory in basins of central and western China. *Pet. Explor. Dev.* **2018**, *45*, 546–560. [CrossRef]
9. Xu, J.W.; Li, J.M.; Wu, Y.Y.; Ding, K.; Jiang, H. Exploration and practice of volume fracturing technology in horizontal well of Mahu tight conglomerate reservoirs. *China Pet. Explor.* **2019**, *24*, 241–249.
10. Li, W.X.; Song, L.; Xi, C.M.; Xie, S.Y.; Rong, K.S. Drilling and completion technology for horizontal well with ultra-Long horizontal section in tight conglomerate reservoir of Xinjiang Mahu oil field. *Xinjiang Oil Gas* **2021**, *17*, 86–91.
11. Ren, L.; Lin, R.; Zhao, J.Z.; Yang, K.W. Simultaneous hydraulic fracturing of ultra-low permeability sandstone reservoirs in China: Mechanism and its field test. *J. Cent. South Univ.* **2015**, *22*, 1427–1436. [CrossRef]
12. Zhuang, Z.; Liu, Z.L.; Wang, T.; Gao, Y. The key mechanical problems on hydraulic fracture in shale. *Chin. Sci. Bull.* **2016**, *61*, 72–81. [CrossRef]
13. Jin, Y.; Cheng, W.; Cheng, M. A review of numerical simulations of hydro-fracking in shale gas reservoir. *Mech. Eng.* **2006**, *38*, 1–9.
14. Cheng, Y. Mechanical interaction of multiple fractures exploring impacts on selection of the spacing number of perforation clusters on horizontal shale gas wells. *Soc. Pet. Eng. J.* **2012**, *17*, 992–1001. [CrossRef]
15. Olson, J.E. Multi-fracture propagation modeling: Applications to hydraulic fracturing in shales and tight gas sands. In Proceedings of the 42nd US Rock Mechanics Symposium (USRMS), San Francisco, CA, USA, 29 June–2 July 2008.
16. Wu, K.; Olson, J.E. Simultaneous multifracture treatments: Fully coupled fluid flow and fracture mechanics for horizontal wells. *SPE J.* **2015**, *20*, 337–346. [CrossRef]

17. Zeng, Q.D.; Yao, J. Numerical simulation of multiple fractures simultaneous propagation in horizontal wells. *Acta Pet. Sin.* **2015**, *36*, 1571–1579.
18. Zhao, J.Z.; Chen, X.Y.; Li, Y.M.; Fu, B.; Xu, W.J. Numerical simulation of multi-stage fracturing and optimization of perforation in a horizontal well. *Pet. Explor. Dev.* **2017**, *44*, 117–124. [CrossRef]
19. Cheng, C.; Bunger, A. Reduced order model for simultaneous growth of multiple closely-spaced radial hydraulic fractures. *J. Comput. Phys.* **2019**, *376*, 228–248. [CrossRef]
20. Ugueto, G.A.; Todea, F.; Daredia, T.; Wojtaszek, M.; Huckabee, P.T.; Reynolds, A.; Laing, C.; Chavarria, J.A. Can you feel the strain? DAS strain fronts for fracture geometry in the BC Montney, Groundbirch. In Proceedings of the SPE Annual Technical Conference and Exhibition, Calgary, AB, Canada, 23 September 2019. SPE 195943.
21. Bunger, A.P.; Zhang, X.; Robert, G.J. Parameters affecting the interaction among closely spaced hydraulic fractures. *SPE J.* **2012**, *17*, 292–306. [CrossRef]
22. Mcclure, M.; Picone, M.; Fowler, G.; Ratcliff, D.; Kang, C.; Medam, S.; Frantz, J. Nuances and frequently asked questions in field scale hydraulic fracture modeling. In Proceedings of the SPE Hydraulic Fracturing Technology Conference and Exhibition, The Woodlands, TX, USA, 1 February 2020. SPE 199726.
23. Cramer, D.D. The application of limited-entry techniques in massive hydraulic fracturing treatments. In Proceedings of the SPE production operations symposium, Oklahoma City, OK, USA, 8–10 March 1987. SPE-16189-MS.
24. Harris, P.C.; Pippin, P.M. High-Rate foam fracturing: Fluid friction and perforation erosion. *SPE Prod Fac.* **2020**, *15*, 27–32. [CrossRef]
25. Kim, G.H.; Wang, J.Y. Interpretation of hydraulic fracturing pressure in low-permeability gas formations. In Proceedings of the SPE Production and operations symposium, Oklahoma City, OK, USA, 27–29 March 2010. SPE-141525-MS.
26. Chen, M.; Zhang, S.; Zhou, T.; Ma, X.; Zou, Y. Optimization of In-Stage Diversion to Promote Uniform Planar Multifracture Propagation: A Numerical Study. *SPE J.* **2020**, *25*, 3091–3110. [CrossRef]
27. Churchill, S.W. Friction-factor equation spans all fluid-flow regimes. *Chem. Eng.* **1977**, *84*, 91–92.
28. Crump, J.; Conway, M. Effects of perforation-entry friction on bottomhole treating analysis. *J. Pet. Technol.* **1988**, *40*, 1041–1048. [CrossRef]
29. Batchelor, G.K.; Hunt, G.T. An Introduction to Fluid Dynamics. In *Appendices*; The Mathematical Gazette: New York, NY, USA, 1968.
30. Valko, P.; Economides, M.J. *Hydraulic Fracture Mechanics*; Wiley: New York, NY, USA, 1995.
31. Sneddon, I.N. The distribution of stress in the neighbourhood of a crack in an elastic solid. *P. Roy. Soc.* **1946**, *187*, 229–260.
32. Chen, M.; Zhang, S.C.; Ma, X.F.; Zhou, T.; Zou, Y. A semi-analytical model for predicting fluid partitioning among multiple hydraulic fractures from a horizontal well. *J. Pet. Sci. Eng.* **2018**, *171*, 1041–1051. [CrossRef]
33. Dontsov, E.V.; Peirce, A.P. A non-singular integral equation formulation to analyze multiscale behavior in semi-infinite hydraulic fractures. *J. Fluid Mech.* **2015**, *781*, 248–254. [CrossRef]
34. Crouch, S.L.; Starfield, A.M. Boundary element methods in solid mechanics: With applications in rock mechanics and geological engineering. In *New South Wales*; Allen & Unwin: Crows Nest, Australia, 1983.
35. Adachi, J.; Siebrits, E.; Peirce, A.; Desroches, J. Computer Simulation of Hydraulic Fractures. *Int. J. Rock Mech. Min. Sci.* **2007**, *44*, 739–757. [CrossRef]
36. Gale, J.F.; Reed, R.M.; Holder, J. Natural fractures in the Barnett shale and their importance for hydraulic fracture treatments. *AAPG Bull.* **2007**, *91*, 603–622. [CrossRef]